Surface atomic order of compound III-V semiconductor alloys at finite temperature

John C. Thomas,[1] Joanna Mirecki Millunchick,[1] Normand A. Modine,[2] and Anton Van der Ven[1,*]
[1]*Department of Materials Science and Engineering, University of Michigan, Ann Arbor, Michigan 48109, USA*
[2]*Center for Integrated Nanotechnologies, Sandia National Laboratories, Albuquerque, New Mexico 87185, USA*
(Received 4 June 2009; revised manuscript received 20 July 2009; published 17 September 2009)

We investigate the role of alloying, atomic-size mismatch strain, and thermal effects on ordering and reconstruction stability of As-rich (2×4) surfaces on $(In_xGa_{1-x})As$ (001) ternary III-V alloys (in the dilute limit) using a first-principles cluster-expansion and Monte Carlo simulations. The cluster expansion accounts for configurational degrees of freedom associated with As dimer adsorption/desorption as well as Ga-In disorder in subsurface cation sites. We analyze the $\alpha2(2\times4)$-$\beta2(2\times4)$ transition at finite temperature and directly examine the entropy and cation-site filling in both reconstructions. A compositionally dependent "zigzag" ordering of dimers in the $\alpha2(2\times4)$ is predicted as well as a hybrid $\alpha2(2\times4)$-$\beta2(2\times4)$ reconstruction, found to be stable in a reasonably large chemical-potential range. The hybrid dimer ordering drives pronounced nanoscale composition modulation of surface cations.

DOI: 10.1103/PhysRevB.80.125315 PACS number(s): 68.35.Md, 68.35.B−, 68.55.−a, 68.60.Dv

I. INTRODUCTION

Surface reconstructions have been shown to play a significant role in epitaxial growth,[1] catalysis,[2] oxide formation,[3] and magnetic domain ordering.[4] These reconstructions form due to strong chemical, elastic, and electrostatic interactions that arise from the directional orbitals of valence electrons at covalently bonded surfaces. These interactions drive a reorganization and rebonding of surface atoms, minimizing the surface free energy. The type of reconstruction present at a surface is thought to affect surface segregation and interface abruptness at semiconductor heterojunctions[5] and can have a measurable effect on heterojunction device I-V response.[6] Reconstructions have also been implicated in inducing sublattice ordering perpendicular to growth during epitaxy[7] whereby surface ordering of segregated alloying elements becomes kinetically trapped in the bulk as the crystal grows. The resultant structures have an altered band-gap relative to the disordered bulk alloy, as well as anisotropic electronic properties.[8] Of particular importance is mounting evidence that surface morphology and surface reconstruction are thermodynamically and kinetically linked,[9] which has significant implications for nanostructural self-assembly.

Rigorous theoretical study of surface reconstructions poses a number of challenges. The range of thermodynamically stable reconstructions that may form on a given surface resides in a very high-dimensional phase space, defined by the structural and configurational degrees of freedom of the system. To complicate matters, the directional bonding, along with the limited number of bonding neighbors at the surface, leads to lower symmetries, reduced atomic coordination, and a larger periodic repeat unit relative to the bulk.

In device design and other applications it is often necessary to alloy two or more compounds to engineer a material within a set of desired parameters. This significantly increases the dimensionality of the associated phase space by creating new configurational degrees of freedom associated with the many possible ways of arranging the alloy constituents over their sublattice sites. In addition, alloying may introduce interactions arising from atomic-size mismatch strain, which is present if the alloy constituent species have significantly different bonding radii.[10] The local strain fields arising from atomic-size mismatch may interact strongly over distances of several bond lengths to induce correlations between the occupancies of non-neighboring sites. Because of these and other effects that necessitate the sampling of many configurations and large length scales, comprehensive stability studies of realistic alloyed covalent surface systems have only recently become possible.

In this paper, we study disorder in surface reconstructions arising from alloying and finite temperature effects using a first-principles cluster-expansion and Monte Carlo (MC) simulations. We focus on a prototypical surface of a ternary III-V semiconductor alloy in order to understand the role that alloying and atomic-size mismatch strain play in surface reconstruction stability and short-range order at covalent surfaces. We choose to consider a thin layer of InAs alloyed on a zinc-blende GaAs (001) substrate since this system is relatively well studied and allows us to examine the role of atomic-size mismatch on surface order at finite temperature due to the large cation size difference between In and Ga.

A. InGaAs (2×4) reconstruction

To model alloying and local strain effects we focus on a specific class of reconstruction observed in GaAs and InAs, encompassing the $\alpha2(2\times4)$ and $\beta2(2\times4)$ reconstructions[11,12] (Fig. 1). They are common to many III-V compounds and possess several shared structural features. The most notable of these are the *dimer row* and the *trench*. The dimer row is the highest feature of the unit cell and consists of either one or two As dimers (which we refer to as *row dimers*) while the trench is one atomic bilayer below the dimer row and contains a single As dimer (the *trench dimer*). The $\alpha2(2\times4)$ and $\beta2(2\times4)$ differ from each other only in that the $\alpha2(2\times4)$ has one row dimer, whereas the $\beta2(2\times4)$ has two.

The $\alpha2(2\times4)$ and $\beta2(2\times4)$ reconstructions have been shown through experiment and first-principles studies to be stable over a continuous range of arsenic chemical potential

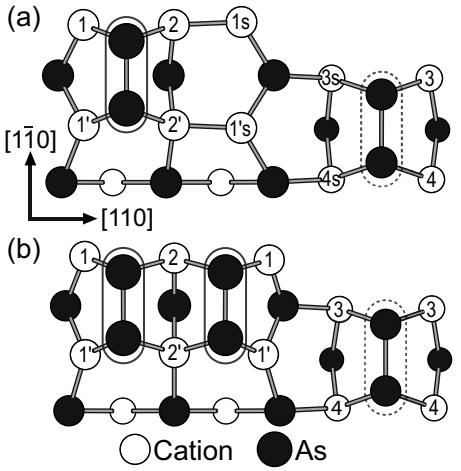

FIG. 1. (a) The $\alpha 2(2\times4)$ and (b) $\beta 2(2\times4)$ reconstructions. Cation sites under consideration are labeled according to symmetric equivalence, assuming periodicity of the unit cell. Solid ellipses indicate row dimers and dashed ellipses indicate the trench dimer.

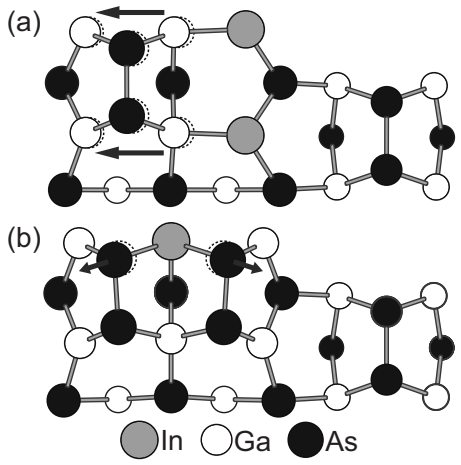

FIG. 2. An illustration of lattice distortion due to atomic-size mismatch upon the substitution of In on the cation sublattice; dashed circles represent atomic positions before substitution. Atom positions were determined via energy minimization from first principles. (a) In the $\alpha 2(2\times4)$ size mismatch can relieve strain inherent in cation-cation backbonds, allowing the surrounding structure to relax to positions approximate to those of the pure GaAs $\beta 2(2\times4)$. (b) In the $\beta 2(2\times4)$ size mismatch leads to significant distortion of the lattice.

on InAs (001)[13] and on GaAs (001),[14] although $\alpha 2(2\times4)$ is predicted to be only marginally stable on the GaAs surface. Alloying GaAs with In, however, appears to stabilize the $\alpha 2(2\times4)$. In work by Krzyzewski *et al.*,[15] which images the InAs wetting layer on GaAs, the $\alpha 2(2\times4)$ appears to occur along with the $\beta 2(2\times4)$. Also, the $\alpha 2(2\times4)$ is predicted to be stabilized upon surface alloying at the $In_{0.5}Ga_{0.5}As$ lattice parameter.[16] Because of these observations and predictions, we can consider these two reconstructions independently from other stable reconstructions within chemical potential intervals near the $\alpha 2(2\times4)$-$\beta 2(2\times4)$ transition.

To study the transition between $\alpha 2(2\times4)$ and $\beta 2(2\times4)$ at finite temperature it is necessary to first identify important configurational degrees of freedom. At the surface, as in the bulk crystal, we distinguish between an anion sublattice and a cation sublattice. The anion sublattice, which we shall refer to here as the *dimer sublattice*, consists of the As row dimers. The $\alpha 2(2\times4)$ and $\beta 2(2\times4)$ reconstructions are formed by placing one and two dimers per unit cell, respectively, on the row dimer sites. The $\beta 2(2\times4)$ reconstruction does not exhibit configurational degrees of freedom on the dimer sublattice as all its row dimer sites are occupied. In the $\alpha 2(2\times4)$ reconstruction, however, half the row dimer sites are unoccupied, allowing for a large number of surface dimer arrangements and thereby creating the potential for substantial disorder at finite temperature. A row dimer coverage of less than 50% must have some unit cells without any row dimers in violation of the electron counting rule.[17] Regions where this occurs are assumed to be unphysical and are indicated as such in the results that follow. The cation sublattice is comprised of the six surface cation sites (those directly below the dimer row) and four trench cation sites (those directly below the trench dimer), which correspond to the labeled cation sites of Fig. 1. These sites take either a Ga or In, providing the potential for surface alloying. We limit consideration to these ten cation sites because the substitutional energy of other subsurface sites is significantly higher, as determined from density-functional theory (DFT) calculations by Cho *et al.*[18] and confirmed by our own calculations. This result reflects experimental observations that show a tendency for In to surface segregate on GaAs (001).[19]

Together the dimer and cation sublattices form our surface model and can be viewed as a thermodynamic system that equilibrates with a gas phase and a bulk GaAs phase having a dilute concentration of In. The thermodynamic boundary conditions of the surface are therefore constant temperature and chemical potentials.

B. Atomic-size mismatch strain

Atomic-size mismatch strain arises when an atomic species with a large bond radius is substituted on the crystalline sites of a species with a smaller bond radius or vice versa. In the case of large mismatch, the substitution typically causes phase separation or ordering of the bulk alloy, except in the dilute limit. However, at two-dimensional interfaces or surfaces, mismatch strain enhances intermixing between species which are otherwise immiscible[20,21] to the extent of inducing surface order.[22] In the system under consideration, In is the larger species with a bond radius 7% larger than that of Ga. Substituting In for Ga on a GaAs surface compresses surrounding bonds, creating a local strain field. The strain fields resulting from alloy substitution interact over distances of several bond lengths to give rise to short-range site correlations or periodic orderings not present in the unalloyed system.

As an illustration, consider the substitution of an In atom between the two dimers of the $\beta 2(2\times4)$ [Fig. 2(b)]. DFT calculations predict that it distorts the lattice, moving the dimers out and away from each other. Alternatively, In atoms substituted opposite the lone row dimer of the $\alpha 2(2\times4)$ [Fig. 2(a)] relieve tensile stress inherent in the Ga-Ga backbonds, allowing the row dimer and the surface Ga atoms

below it to relax toward their corresponding positions in the $\beta 2(2\times4)$. Thus, at dilute concentrations inserting an In atom into the $\alpha 2(2\times4)$ is energetically preferred to inserting an In atom into the $\beta 2(2\times4)$.

Recent work by Bickel *et al.*[10] examined this mechanism as an explanation for experimentally observed local order of the $\alpha 2(2\times4)$. In that first-principles study, they found that the $\alpha 2(2\times4)$ ground states at low and intermediate In concentration have a "zigzag" arrangement of the dimer row along the $[1\bar{1}0]$ axis. This was attributed to the strong repulsive interaction between the size-mismatched In atoms and the lone $\alpha 2(2\times4)$ row dimer, which causes In pairs to occupy the sites opposite the dimer. Furthermore, the tendency of In atoms to maximize their distance from other In atoms results in In pairs and row dimers to orient in an alternating pattern along $[1\bar{1}0]$. This paper builds upon that work by considering the trench cation sites in addition to the surface cation sites and by exploring the transition between the $\alpha 2(2\times4)$ and $\beta 2(2\times4)$ reconstructions at finite temperature. We consider interactions among row dimers, In, and Ga, and examine finite temperature effects on surface stability using a cluster expansion parameterized by first-principles energy calculations within Monte Carlo simulations.

By using these techniques to explore the configurational phase space of the $\alpha 2(2\times4)$ and $\beta 2(2\times4)$ on InAs/GaAs (001), we have identified several basic rules for size mismatch interactions that play a significant role in determining the equilibrium configuration of the system. Understanding these prevailing effects is useful for developing intuition about the system, as one or more of them are evident in all of the results presented in this paper. They are discussed in greater detail in Sec. III but are summarized as follows:

It is energetically unfavorable for row dimers to directly bond to In atoms. Because the adsorption of an As dimer constrains the positions of underlying sites, substitution of larger In atoms is energetically unfavorable in surface cation sites bonding to the dimer.

High-symmetry cation sites accept In more readily. Although the first guideline takes precedence at lower As and cation chemical potentials, the sites that sit along the $(1\bar{1}0)$ mirror plane are energetically preferred for In substitution in the $\beta 2(2\times4)$. Because they have higher symmetry than the other cation sites, the cation and dimer sublattices relax more uniformly to accommodate In at these sites while allowing relatively large distances between In atoms.

Row dimers cause compressive strain at a subset of cation trench sites. Row dimers force the underlying cation sites to relax toward each other, resulting in compressive strain around certain sites in the trench, labeled by a 3 in Fig. 1. This significantly increases the substitution energy of these sites relative to similar sites with no nearby row dimer, as is the case near the dimer vacancy of the $\alpha 2(2\times4)$.

Low-energy configurations maximize distance between In atoms. Because of their large size relative to Ga, interactions between In atoms are repulsive. For many surface stoichiometries the previous three guidelines usually dominate but the mutual repulsion of In is important in the dilute In limit or over the range of several unit cells, where dimers and In atoms can arrange themselves such that the first guideline above is satisfied while simultaneously ensuring maximal or near-maximal distance between In atoms.

II. METHODOLOGY

Of primary interest is the dependence of surface order on alloy stoichiometry and temperature, which motivates the development of an effective Hamiltonian within the cluster-expansion formalism to account for the configurational degrees of freedom identified above. The cluster expansion of the configurational energy is chosen as it is a compact and easily evaluated effective Hamiltonian and, with Monte Carlo, allows full consideration of thermal effects due to configurational entropy. These entropic effects, which have hitherto been unaccounted for in most models of this and similar alloyed compound semiconductor systems, have considerable ramifications for phase stability and order in multicomponent systems at typical growth temperatures.

A. Cluster expansion

Our effective Hamiltonian must fully capture the energetics of species substitution on the cation sublattice, dimer adsorption on the dimer sublattice, and coupling of the two sublattices arising from local relaxations and electronic structure. The cluster-expansion formalism is uniquely suited for these provisions.

In the cluster-expansion formalism, the occupancy of each site of the lattice is described by an occupation variable. For a substitutional cation site, i, we introduce the occupation variable σ_i, which takes a value of $+1(-1)$ if the site is occupied by In (Ga). Likewise, for an adsorptive dimer site, j, the occupation variable δ_j has a value $+1$ if the site is occupied by a dimer and -1 if the site is vacant. These conventions allow a complete description of the configurational state of the surface using the set of occupation variables of all surface sites on the lattice, denoted by $\vec{\sigma}, \vec{\delta}$.

For each cluster of sites, η, corresponding to point clusters, pair clusters, triplet clusters, etc., we define a cluster function, $\Gamma_\eta(\vec{\sigma}, \vec{\delta})$, which is the product of all σ_i and δ_j for sites i and j contained in η. Formally,

$$\Gamma_\eta(\vec{\sigma}, \vec{\delta}) = \prod_{j\in\eta} \prod_{i\in\eta} \sigma_i \delta_j \tag{1}$$

with the stipulation that the product over the empty set is 1. It has been shown that the set of all cluster functions of a lattice form a complete and orthonormal basis.[23] Hence it is possible to rigorously expand any property that depends on the arrangement of dimers and cations as a linear combination of cluster functions.[23–25] The fully relaxed configurational energy for a two-sublattice system takes the form[26]

$$E(\vec{\sigma}, \vec{\delta}) = \sum_{\{\eta\}} V_\eta \Gamma_\eta(\vec{\sigma}, \vec{\delta}), \tag{2}$$

where V_η is a constant coefficient and is the effective cluster interaction (ECI) associated with cluster η. The ECI of the "empty cluster" is nonzero. A similar approach was used to study oxygen adsorption-induced surface segregation on the Pt-Ru alloy surface.[27]

In principle, the cluster expansion must extend over all clusters to exactly express a configurationally dependent quantity due to the completeness of the basis set. In practice, it is possible to truncate the cluster expansion, only including those clusters smaller than some physically relevant length scale of the system. Likewise, it is typically unnecessary to include clusters containing more than three or four sites. Only a small fraction of the ECI in Eq. (2) are found to be independent due to the symmetric equivalence of most clusters. We can then parameterize the various ECI of this simplified expression using a manageably small number of configurational energies calculated directly from first principles. Consequently, the cluster expansion presents a compact and computationally efficient method for predicting the configurational energy of large systems.

We parameterized a cluster expansion of the form given in Eq. (2) using a training set of 378 configurational energies calculated using DFT as implemented in the VASP code[28] with ultrasoft pseudopotentials[29] within the local-density approximation (LDA), using the Ceperley-Alder correlation functional[30] as parameterized by Perdew and Zunger.[31] To calculate these energies a slab of six bulklike atomic bilayers of GaAs was used to approximate the GaAs substrate, terminated above the top layer by the reconstructed surface. The bottom atomic bilayer was fixed at the bulk GaAs lattice parameter, as determined by LDA DFT. Atoms in all other layers, and in the reconstructed surface, were allowed to relax to their stable energy minima. The slab was separated from its periodic image by approximately 12 Å of vacuum and its bottom surface was passivated by a layer of pseudohydrogen, with nuclear charge $Z=0.75$, to minimize electrostatic self-interaction across the vacuum layer.

A genetic algorithm was used to select clusters to include in the basis set of the cluster expansion[32] with the goal of minimizing the leave-one-out cross-validation score.[33] ECI for a given basis set were determined using a least-squares fit. Figure 3 illustrates the values of the resulting ECI for site occupancy as well as pair, triplet, and quadruplet interactions. Due to the low symmetry of the combined dimer and cation sublattices, 62 clusters were included in the fit, including the empty cluster, seven point clusters, 39 pair clusters, 14 triplet clusters, and one quadruplet cluster. The cross-validation score of the basis set is 2.02 meV per surface site and the final least-squares fit has a root-mean-squared error of 1.55 meV per surface site. In the optimized basis set the only interdimer interaction retained is that of the nearest-neighbor dimer pair that exists within the unit cell. This pair interaction is the strongest one found for the system and describes a large repulsive interaction between dimer nearest neighbors. Despite this large nearest-neighbor dimer interaction, the dimer row is the highest feature of the unit cell, making row dimers quite isolated from those of neighboring unit cells and minimizing chemical or elastic interactions between them. Hence longer range interdimer interactions are negligible. Of the remaining multibody interactions, 31 involve only cation sites and 22 involve both cation and dimer sites. Figure 4 shows the 22 clusters having the strongest interactions in the system, as measured by the magnitude of their ECI. In interpreting values of ECI it is useful to refer to Eq. (2), from which we see that a negative pair ECI

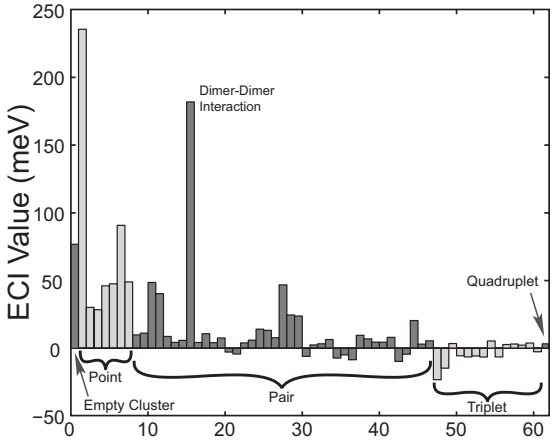

FIG. 3. The relative magnitudes of all ECI included in the cluster expansion. ECI are grouped by number of sites included; within each group they are ordered by increasing interaction length. Site ECI are ordered with the dimer first and then 1, 1′, etc., as labeled in Fig. 1(a).

indicates an energetically preferred interaction between like species. The physical significances of ECI of triplet and larger clusters are somewhat harder to interpret since there are eight possible configurations of a triplet cluster and 2^n possibilities for n-body clusters. Of particular interest among the interactions shown in Fig. 4 are the dimer-dimer interaction, the interactions between the row dimer and the cation sites that bond directly to it, and the interaction between the row dimer and the nearest trench cation site, as the effects of these are especially apparent in the Monte Carlo results. Also, note that there are significant interactions which act directly across the trench, despite the expectation that the trench minimizes interactions between neighboring unit cells along [110].

The training set used to fit the ECI consists of a range of configurations of variously shaped (2×4), (2×8), and (4×4) supercells, selected using a number of metrics intended to ensure that the configurational phase space was evenly sampled and that the ECI of candidate clusters were sufficiently overdetermined. Additionally, configurations that were found to be ground states of preliminary cluster expansions were added to the training set in an iterative process to test the accuracy of the cluster expansion and optimize its ability to predict ground-state configurations. For the (2×4) supercell, brute force enumeration of configurations was used to identify ground-state structures. However, because the number of possible configurations grows exponentially with supercell size ($\propto 2^{12n}$, where n is the number of unit cells), simulated annealing must be used to identify ground-state configurations of larger supercells. This is accomplished by applying Monte Carlo simulations to a preliminary cluster expansion in an appropriately sized supercell at fixed chemical potentials and starting at a high temperature relative to the site interactions. The temperature is gradually reduced until the supercell configuration no longer changes. The configuration with the lowest energy during the simulated annealing run is recorded and after repeating the process for the relevant range of chemical potentials, all such configurations are compared to determine the ground states.

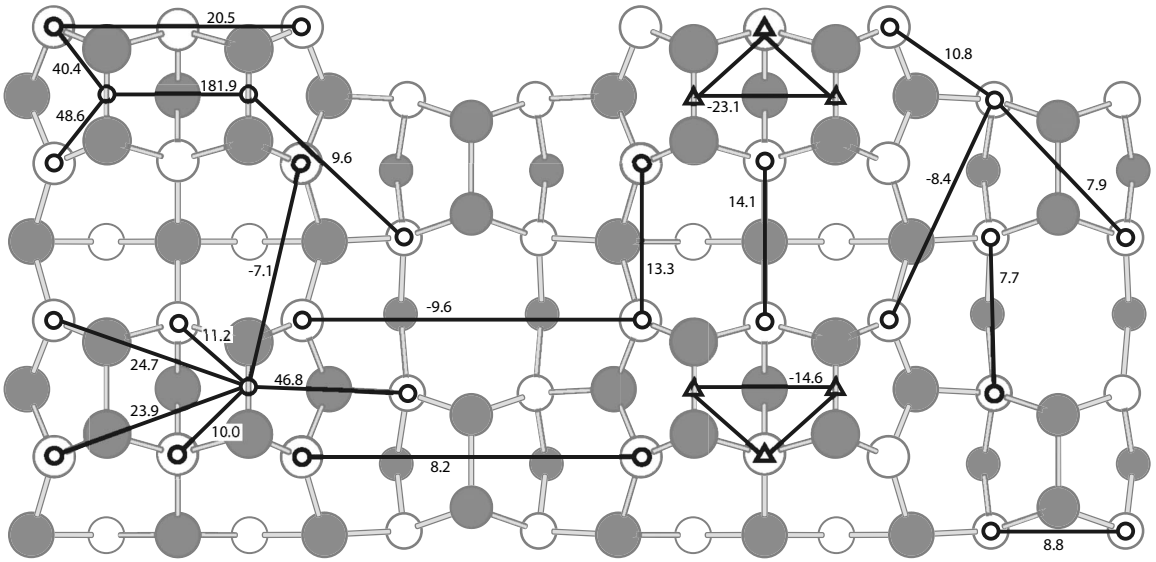

FIG. 4. Diagram of the 22 strongest cluster interactions with ECI indicated in meV. Lines joining open circles represent pair interactions; lines joining open triangles represent triplet interactions. Refer to Fig. 1(a) for symmetrically equivalent cation sites. All dimer sites are symmetrically equivalent.

B. Simulation details

Although zero-Kelvin phase diagrams can be constructed directly from first-principles energies of a library of configurations or by finding ground states of the cluster expansion, these phase diagrams are based on energies of relatively well-ordered reconstructions and have sharp boundaries separating different reconstructions in chemical-potential space. Entropy arising from configurational disorder becomes important with increasing temperature, affecting phase boundaries and changing the nature of thermodynamic transitions compared to zero-Kelvin predictions. In systems with significant thermally induced disorder, these effects complicate experimental characterization informed by zero Kelvin predictions. In order to incorporate temperature effects and make physically useful predictions of experimental results via the calculation of ensemble averages, we have applied the Metropolis Monte Carlo algorithm[34] to the cluster expansion of Sec. II A. Simulations are conducted within the grand canonical ensemble with the temperature and the chemical potentials of the two sublattices as independent thermodynamic boundary conditions. As an adsorptive species, the As chemical potential, μ_{As}, is independently controlled. Conversely, since In and Ga are substitutional species, only the *relative* cation chemical potential, $\Delta\mu_{cat}=\mu_{\mathrm{In}}-\mu_{\mathrm{Ga}}$, has an effect on the equilibrium state of the system if the number of cation sites remain fixed.

To facilitate comparison with experiment, we use as reference states the rhombohedral *A*7 phase of bulk As, fully relaxed bulk GaAs and fully relaxed InAs. With this choice of reference states, $\mu_{\mathrm{As}}>0$ results in the formation of bulk As on the surface in thermodynamic equilibrium. For the cation sublattice, a very low (negative) value of $\Delta\mu_{cat}$ corresponds to a state where the surface is in equilibrium with bulk GaAs having a dilute concentration of In. The surface can equilibrate at a significantly higher In concentration than exists in the bulk because at low $\Delta\mu_{cat}$ in an epitaxially grown alloy film, In will tend to segregate to the surface due to atomic-size effects, as well as the lower surface free energy of InAs. An increasing value of $\Delta\mu_{cat}$ approaching zero physically corresponds to the surface being in equilibrium with an increasingly nondilute $\mathrm{In}_x\mathrm{Ga}_{1-x}\mathrm{As}$ alloy. However, since the total-energy calculations used to parameterize the cluster expansion were performed on GaAs slabs, with In occupying only surface cation sites, high values of $\Delta\mu_{cat}$ in our model system correspond more accurately to experimental conditions where a partial monolayer of InAs is directly deposited on GaAs. This is a metastable equilibrium where excess In at the surface is prevented from diffusing into the bulk due to sluggish kinetics.

Grand canonical Monte Carlo simulations were performed at several temperatures and on a dense grid of chemical-potential values for μ_{As} and $\Delta\mu_{cat}$ that stabilize the full range of As and In compositions in our surface model. The Monte Carlo simulation cell consisted of 288 primitive cells (a square 24×12 lattice with periodic boundary conditions) for a total of 2880 cation sites and 576 dimer sites. At each point the system was equilibrated over 3000 MC passes (each site is visited 3000 times on average) and ensemble averages were tracked over the following 5000 MC passes. High-resolution data were collected along chemical-potential trajectories corresponding to pure $\alpha2(2\times4)$ and $\beta2(2\times4)$ surfaces. For the former, the trajectory along which dimer coverage is exactly 50% was interpolated from exploratory MC runs. For the latter, the same contour was used but shifted to a higher As chemical potential such that only the $\beta2(2\times4)$ was sampled. Data along the trajectories were acquired using a 72×35 lattice over 11 000 MC steps after 5000 MC steps of equilibration.

Various second derivatives of the free energy with respect to independent thermodynamic parameters were calculated directly at each point from fluctuations of extensive quantities. The relation between fluctuations and second derivatives of the free energy is obtained by explicitly taking the second

derivative of the free energy relevant to the surface. The free energy is obtained by applying a Legendre transform to the internal energy E of the surface with respect to all intensive experimentally controlled variables (i.e., T, μ_{As}, and $\Delta\mu_{cat}$) according to

$$\Phi = E - TS - \mu_{\mathrm{As}}N_{\mathrm{As}} - \Delta\mu_{cat}N_{\mathrm{In}}. \tag{3}$$

This free energy is related to the statistical mechanical partition function Z by $\Phi = -k_B T \ln(Z)$, where Z is the grand canonical partition function, defined by the sum over all configurational microstates s,

$$Z = \sum_s \exp\left[-\frac{(E - \mu_{\mathrm{As}}N_{\mathrm{As}} - \Delta\mu_{cat}N_{\mathrm{In}})_s}{k_B T}\right]. \tag{4}$$

Explicit differentiation of the statistical mechanical free energy yields an expression relating its second derivatives to the variances of extensive quantities. As an example, the chemical susceptibility, χ_{ij}, defined as the derivative of N_j with respect to the chemical potential μ_i, where i and j are either As or In, is equal to the second derivative of the free energy Φ and can be expressed in terms of fluctuations in the number of atoms of species i and j according to

$$\chi_{ij} = \frac{\partial^2\Phi}{\partial\mu_i\,\partial\,\mu_j} = \frac{1}{(k_B T)}(\langle N_i N_j\rangle - \langle N_i\rangle\langle N_j\rangle). \tag{5}$$

The various second derivatives of the free energy are useful in identifying phase boundaries. A discontinuity of the second derivative indicates a first-order transition while a diverging second derivative indicates a second-order transition.

III. RESULTS

A. Surface stability and temperature dependence

One of the most readily interpreted properties of the system is the relative stability of the $\alpha2(2\times4)$ and $\beta2(2\times4)$ reconstructions. Figure 5 shows a surface stability map of the $\alpha2(2\times4)$ and $\beta2(2\times4)$ reconstructions of InAs/GaAs (001) at 100 °C within the physically meaningful chemical-potential ranges. The quantity used to determine the boundary in Fig. 5 is the As dimer chemical susceptibility, $\chi_{\mathrm{As,As}}$, as defined in Eq. (5). We determine from the dimer susceptibility that there is no formal first- or second-order phase transition between the $\alpha2(2\times4)$ and $\beta2(2\times4)$ since there is no clearly visible divergence or discontinuity of $\chi_{\mathrm{As,As}}$. Instead, there is a smooth transition, indicated by a nonsingular maximum in $\chi_{\mathrm{As,As}}$, between $\alpha2(2\times4)$ and $\beta2(2\times4)$ along lines of constant $\Delta\mu_{cat}$. As expected, the $\beta2(2\times4)$ is stable at higher μ_{As} and the $\alpha2(2\times4)$ is stable at lower μ_{As} since the $\beta2(2\times4)$ is more As rich. The black region of Fig. 5 corresponds to the chemical-potential ranges where the $\alpha2(2\times4)$ becomes unstable relative to the unreconstructed surface, which is the limiting case of the configurational model. At this lower extreme of μ_{As} the electron counting rule is violated, resulting in an unphysical situation. Other reconstructions and/or bulk phases not explicitly considered in this work will form at these chemical potentials.

An intriguing trend highlighting the sublattice coupling occurs at fixed μ_{As} with cation chemical potential, $\Delta\mu_{cat}$,

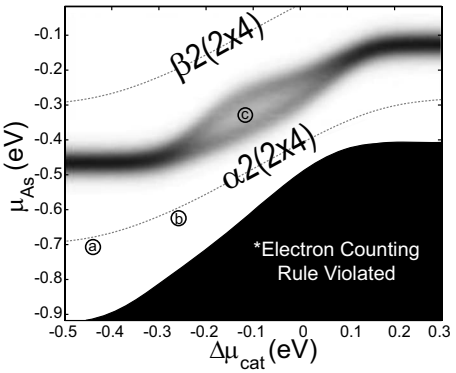

FIG. 5. Surface stability map of the InAs/GaAs (001) surface showing the chemical-potential domains of stability for the $\alpha2(2\times4)$ and $\beta2(2\times4)$ at 100 °C. A small region, labeled (c), exists between the two larger ones where the $h_{\alpha\beta}$, a hybrid of the $\alpha2(2\times4)$ and $\beta2(2\times4)$, is stable. Boundaries are calculated from the dimer chemical susceptibility, with width corresponding to the chemical-potential interval over which the smooth transition between reconstructions occurs. The obscured region is an unphysical limit of the configurational model and corresponds to relative stability of the bulk-terminated surface. Points a, b, and c correspond to microstate snapshots shown in Fig. 10.

allowed to vary freely. Raising $\Delta\mu_{cat}$ results in increased In concentration over the surface sites. A high surface In concentration in turn destabilizes the $\beta2(2\times4)$ via atomic-size mismatch strain interactions in favor of an $\alpha2(2\times4)$ surface. This phenomenon is seen most clearly in Fig. 6(a), which shows the increase in In concentration and resultant decrease in dimer coverage as $\Delta\mu_{cat}$ is increased and μ_{As} is held constant. Figure 6(b) shows a related but weaker effect, where there is a slight decrease in In concentration during the transition from the $\alpha2(2\times4)$ (50% dimer coverage) to the $\beta2(2\times4)$ (100% dimer coverage) at fixed $\Delta\mu_{cat}$. The reconstruction destabilization is due to the coupling between the cation and As sublattices as accounted for by the cluster expansion and is attributed to the atomic-size mismatch strain as illustrated in Fig. 2. As was described by the first guideline for size mismatch interaction detailed in Sec. I B, the substitution of In in the $\beta2(2\times4)$ results in a nontrivial displacement of the row dimers, straining the bonds between row dimers and cations. By contrast, substitution of In in the $\alpha2(2\times4)$ results in comparatively little distortion of the lattice relative to the pure GaAs $\beta2(2\times4)$ lattice positions, reducing energetically unfavorable strain fields.

In addition to the regions of $\alpha2(2\times4)$ and $\beta2(2\times4)$, Fig. 5 also shows a region within the $\alpha2(2\times4)$-$\beta2(2\times4)$ transition where $\chi_{\mathrm{As,As}}$ is not maximal. This corresponds to a hybrid reconstruction comprised of both the $\alpha2(2\times4)$ and $\beta2(2\times4)$ reconstructions, which we will refer to as $h_{\alpha\beta}$. Although the $h_{\alpha\beta}$ is reminiscent of a nanoscale phase coexistence, there is no possibility of phase coexistence since the system lacks a first-order phase transition. Instead, it is an independent surface ordering with corresponding zero-temperature configurational ground states. There is in fact a series of zero-temperature hybrid reconstruction ground states near 75% dimer coverage over a range of In compositions. At finite temperature the hybrid surface is stable over a

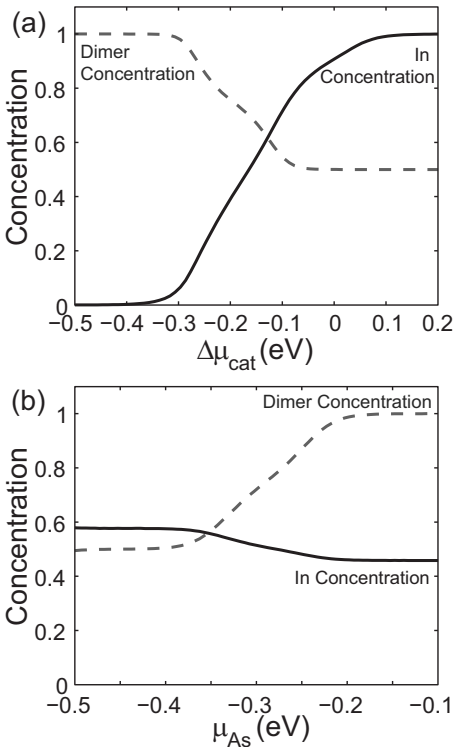

FIG. 6. The dimer and In concentrations at 100° (a) along a line of constant cation chemical potential with $\Delta\mu_{\mathrm{cat}}$ fixed at −6 meV and (b) along a line of constant As chemical potential with μ_{As} fixed at −313 meV. Chemical potentials are measured on the same axes as Fig. 5.

range of In and dimer composition, extending from approximately 30–55 % surface In concentration and 70–80 % dimer coverage at 100 °C, although it is most stable at 45% surface In and 75% dimer coverage, where there is a local minimum in χ_{As_2}. The predicted ground-state configurations of the hybrid reconstruction are formed by alternating $\alpha 2(2\times 4)$ and $\beta 2(2\times 4)$ unit cells along both [110] and $[1\bar{1}0]$, having a 4×8 or a centered 4×8 primitive cell, depending on the relative orientations of the $\alpha 2(2\times 4)$ row dimers. However, at typical growth temperatures (500 °C), the $h_{\alpha\beta}$ surface shows significant disorder, although the primitive cell can still often be identified over the length scale of several (2×4) unit cells, suggesting that the hybrid surface can readily tolerate defects at finite temperatures.

With Monte Carlo simulations within the grand canonical ensemble, we can obtain a variety of thermodynamic properties at finite temperature, including the free energy Φ and the entropy S, through free-energy integration. By applying the combined first and second laws of thermodynamics, we write the total differential of the free energy as

$$d\Phi = -SdT - N_{\mathrm{As}}d\mu_{\mathrm{As}} - N_{\mathrm{In}}d\Delta\mu_{cat}, \tag{6}$$

which is easily integrated at constant temperature ($dT=0$). The grand canonical energy at one of the extremes of composition where configurational entropy is absent (e.g., $x_{\mathrm{As}}=x_{\mathrm{In}}=1$) is used as a reference since the free energy Φ_0 at this point is equal to the grand canonical energy, $\Phi_0=E-\mu_{\mathrm{As}}N_{\mathrm{As}}-\Delta\mu_{cat}N_{\mathrm{In}}$. Once Φ is determined, we solve Eq. (3) for TS, which is the entropic contribution to the free energy arising from configurational excitations.

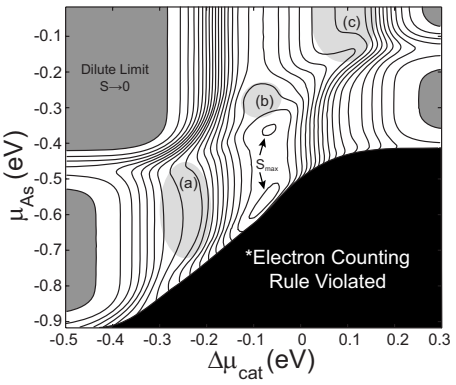

FIG. 7. Configurational entropy at 100 °C, illustrating adiabatic contours. Regions of low contour density indicate either significant order or disorder. This occurs as a limiting case at chemical-potential extremes (shaded dark gray) but several other nontrivial cases occur (light gray): (a) the zigzag ordering of the $\alpha 2(2\times 4)$, (b) the $h_{\alpha\beta}$ hybrid reconstruction, and (c) local ordering of the cation sublattice in the $\beta 2(2\times 4)$. As in Fig. 5, the black region indicates an unphysical limiting case of the configurational model.

Figure 7 illustrates the configurational entropy of the surface as a function of μ_{As} and $\Delta\mu_{cat}$. The contours follow lines of constant entropy and thus are adiabatic chemical-potential contours. The entropy is highest near 50% composition on both sublattices due to purely combinatoric reasons. The two entropy maxima shown in Fig. 7 are slightly off stoichiometry since at low temperatures the system is constrained to the $\alpha 2(2\times 4)$ at 50% dimer coverage. By going slightly above and below 50% dimer concentration, and thus approaching the transitions away from the $\alpha 2(2\times 4)$, fluctuations in dimer concentration increase, reflected by an increase in entropy.

Generally, regions of significant order or disorder are expected where the density of adiabatic contours is low, as the entropy is relatively flat with respect to changes in μ_{As} and $\Delta\mu_{cat}$ in these areas. Figure 8 shows the entropy calculated along the chemical-potential trajectories, shown as dotted lines in Fig. 5, corresponding to pure $\alpha 2(2\times 4)$ and pure $\beta 2(2\times 4)$. It is evident from the entropy along these trajectories, where only a single reconstruction is sampled, that certain surface cation compositions drive a local change in the convexity of the entropy. The most prominent of these composition intervals correspond to chemical-potential regions of visibly decreased adiabat density in Fig. 7 (shaded light gray), further suggesting the occurrence of increased long- or short-range order. These regions deserve special attention and are discussed in detail in Sec. III C. It is also important to note that over most of the range of cation composition, the $\alpha 2(2\times 4)$ has higher entropy than the $\beta 2(2\times 4)$ due to the greater number of possible dimer arrangements on the $\alpha 2(2\times 4)$ surface. The directional nature of the $\alpha 2(2\times 4)$, caused by its single dimer vacancy, allows many distinct arrangements of the dimer sublattice in the $\alpha 2(2\times 4)$, as opposed to just one arrangement of dimers in the $\beta 2(2\times 4)$.

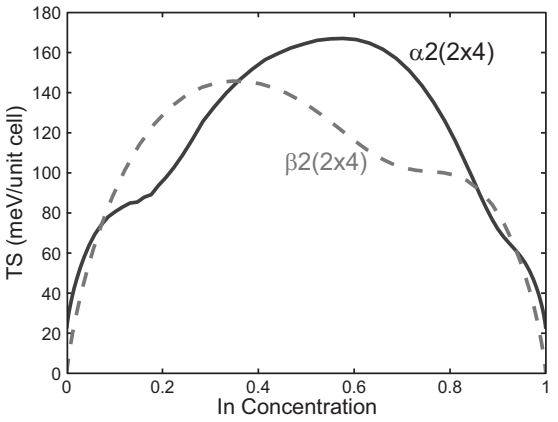

FIG. 8. Entropic contribution to free energy, as a function of In concentration, for the $\alpha 2(2\times4)$ and $\beta 2(2\times4)$ reconstructions at 100 °C. The contribution from the $\alpha 2(2\times4)$ is higher than that of the $\beta 2(2\times4)$ over most of the range of concentration. Intervals where the entropic contribution is suppressed correspond to short-range order.

B. Preferential cation-site filling

To examine the connection between composition and short-range order, we consider the average occupancies of the sites on the cation sublattice. Each of the cation sites of the $\beta 2(2\times4)$ lattice is classified as one of six symmetrically distinct sites, as labeled in Fig. 1(a). This is due to the mirror plane that bisects the reconstruction across the [110] direction. There is no $(1\bar{1}0)$ mirror plane since the trench dimer is shifted by one quarter of a unit cell relative to the row dimers. Energetically similar but symmetrically distinct sites (generally, those whose degeneracy is broken only by the trench dimer) are distinguished by a prime symbol, according to their position relative to the trench dimer. The removal of a dimer from the $\beta 2(2\times4)$ to form the $\alpha 2(2\times4)$ breaks the [110] mirror symmetry, leading to ten fully distinct cation sites. As shown in Fig. 1(b), this allows us to distinguish between those sites which are adjacent to a row dimer and those which are opposite a row dimer (denoted by a "*s*"). Figure 9 shows a comparison of the In concentration of the various symmetrically distinct cation sites for both the $\alpha 2(2\times4)$ [Figs. 9(a) and 9(b)] and $\beta 2(2\times4)$ [Fig. 9(c)] along chemical-potential trajectories corresponding single reconstruction coverage (shown as dashed lines in Fig. 5). The sites are labeled as shown in Fig. 1. The trends displayed for the various sites provide significant intuition about the role of atomic-size mismatch and sublattice coupling.

Type 1 sites. The four surface cation sites that sit on the outside of the dimer row comprise the type 1 sites, as indicated in Fig. 1. Due to the mismatch strain effects illustrated in Fig. 2 and detailed in the first guideline for strain interaction in Sec. I B, sites 1*s* and 1′*s* accommodate In more readily than other sites in the $\alpha 2(2\times4)$, relieving the strain inherent in the cation-cation backbonds of the reconstruction and allowing the single row dimer and surrounding sites to sit closer to the positions occupied in the $\beta 2(2\times4)$. This is reflected in the average site occupancy for the $\alpha 2(2\times4)$, shown in Fig. 9(a). Here, the 1*s* and 1′*s* sites (which are similar to the 1 and 1′ sites but sit opposite the lone row dimer) are nearly fully occupied by In at low average In composition. At low average composition the 1- and 1′-site occupancies are slightly below average due to the very large contribution to the average from the 1*s* and 1′*s* sites. At intermediate and high average composition the 1- and 1′-site occupancies closely follow the average.

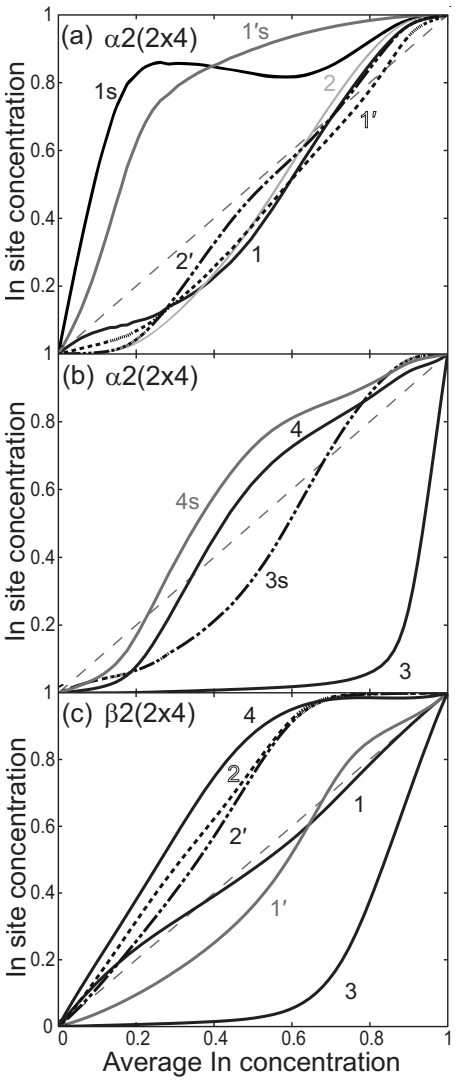

FIG. 9. In occupancy of various cation sites at 100 °C. Site labels correspond to those in Fig. 1. (a) Surface sites and (b) trench sites of the $\alpha 2(2\times4)$, and (c) all sites of the $\beta 2(2\times4)$. In each figure, the dashed line along the 45° is the average In concentration.

In the $\beta 2(2\times4)$ [Fig. 9(c)], there is less preference for type 1 sites to accept In than in the $\alpha 2(2\times4)$ [Fig. 9(a)]. Instead, the site filling remains close to or below the average composition over a wide range of In composition. For average In compositions below approximately 65%, 1 sites are slightly preferred over 1′ sites. This is likely caused by the 1′ site being slightly constrained due to its relative proximity to the trench dimer. The increase in 1′ site filling is concurrent with increased filling of site 3 and because of the strong influence of type 3 sites on the local relaxation of the trench dimer, this may also indicate a causative factor in 1′ site filling overtaking the filling of site 1.

Type 2 sites. The type 2 sites are comprised of the two cation sites that sit between the row dimer sites. Because the type 2 sites are bisected by a mirror plane, the many short-range pair interactions affecting them have mirror symmetry. This leads to a strong coupling with neighboring cation sites as well as with the row dimers.

In the $\alpha 2(2\times 4)$ [Fig. 9(a)], In filling of type 2 sites is suppressed at low In concentration as the highly preferred 1 and $1'$ sites fill. At intermediate and high In concentration, the filling trends of 2 and $2'$ sites closely follow the average In concentration. In the $\beta 2(2\times 4)$ [Fig. 9(c)], the type 2 sites exhibit preferential In filling over the entire range of In concentration. This is mainly due to the relatively low density of type 2 and $2'$ sites, as well as the relatively large distance of these sites from the trench dimer. As stated in the second strain interaction guideline of Sec. I B, proximity tends to increase a site's substitutional energy. Any anisotropy that exists between the 2 and $2'$ sites is likely due to interactions with the trench dimer mediated by the nonuniform occupation of neighboring sites.

Type 3 sites. The type 3 sites lie in the trench and are directly inline with and adjacent to the row dimers along $[1\bar{1}0]$. Although type 3 sites are three atomic monolayers below the row dimer sites, the position of the type 3 sites relative to the row dimer sites results in a strong coupling between row dimer occupation and type 3 substitution energy. The row dimer compressively strains the bonds above and surrounding the adjacent type 3 site, significantly increasing the energy of substituting a large In atom at the site. This is most clearly demonstrated for the $\alpha 2(2\times 4)$, where Fig. 9(b) shows a strong anisotropy between the $3s$ and 3 sites. The 3 site exhibits almost no filling until it is forced to as it becomes the only remaining site for substitution at high $\Delta\mu_{cat}$. By comparison, the $3s$ site is quite low in energy, as evidenced by a site occupation approaching and exceeding the average at moderate to high In composition. In the $\beta 2(2\times 4)$, where both sites adjoin a row dimer, the type 3 sites exhibit almost no substitution until all other sites are more than half filled with In.

Type 4 sites. Although type 4 sites also lie within the trench, they are relatively low in energy and exhibit higher than average In occupation at most In and row dimer concentrations. In the $\alpha 2(2\times 4)$, the type 4 sites readily accept In but filling is delayed at lower concentrations, as filling of the low-energy $1s$ and $1's$ sites takes precedence. There is only minimal interaction with the row dimer, as seen by the very similar filling profiles for $4s$ and 4 sites. This relatively weak coupling to the row dimer sublattice is also very noticeable in the $\beta 2(2\times 4)$, where the type 4 sites fill with even higher precedence, reaching full occupancy at 60% average In concentration. This is mainly due to the large increase in substitutional energy of all other site types when the dimer sublattice is fully occupied.

C. Alloy-driven ordering

Having demonstrated the strong differences in average cation-site occupancy among the various cation sites in Sec. III B, we surmise that in regions of chemical-potential space where these differences are strongest we are likely to observe either long- or short-range ordering on at least the cation sublattice and likely the row dimer sublattice as well. These regions also correspond to changes in the convexity of the entropy illustrated in Figs. 7 and 8. For the $\alpha 2(2\times 4)$ there are two regions where increased short-range order is expected, as determined by these two indicators. One is near 20% In concentration and the other is near 90%, easily visible in Fig. 8. An even stronger suppression of the entropy is observed in the $\beta 2(2\times 4)$ between 60 and 65% In concentration. In addition to these ordered regions in the pure $\alpha 2(2\times 4)$ or $\beta 2(2\times 4)$, there is the thermodynamically stable $h_{\alpha\beta}$ hybrid reconstruction. As stated previously, the $h_{\alpha\beta}$ occurs over a range of In and dimer concentrations and, like the ordered regions of the pure reconstructions, is associated with a change in the convexity of the entropy. By examining correlation functions and instantaneous microstate snapshots of the MC simulation cell, we are able to better understand the significance of these regions.

We obtain a quantitative measure of the short-range order of the dimer sublattice by constructing an order parameter that quantifies the tendency of row dimers in the $\alpha 2(2\times 4)$ to arrange themselves in straight lines along the $[1\bar{1}0]$ axis or to form a zigzag arrangement along $[1\bar{1}0]$. Zigzag ordering has been studied previously in this system using DFT energy calculations[10] and, in the absence of defects, is described by a (4×4) unit cell, shown as an inset in Fig. 11. The dimer sites of Fig. 11 inset are numbered from 1 to 4 and, as defined earlier, the occupation variable of site i is $\delta_i=+1$ for a dimer and $\delta_i=-1$ for a vacancy. We write an expression

$$p_z = (1+\delta_1)(1-\delta_2)(1-\delta_3)(1+\delta_4)/16 \tag{7}$$

such that perfect zigzag ordering (Fig. 11 inset) yields a value of $p_z=1$ while $p_z=0$ otherwise. The ensemble average of p_z then gives the probability that a (4×4) cell has the dimer configuration shown in Fig. 11 for a given set of thermodynamic parameters. Expanding Eq. (7) and taking the ensemble average, we find

$$\langle p_z\rangle = (1-2\langle\delta_1\delta_2\rangle-2\langle\delta_1\delta_3\rangle+2\langle\delta_1\delta_4\rangle+\langle\delta_1\delta_2\delta_3\delta_4\rangle)/16, \tag{8}$$

where terms corresponding to symmetrically equivalent clusters have been combined or cancel each other. Noting that the configuration of Fig. 11 (inset) is symmetrically equivalent to its mirror across (110) (i.e., the pattern of black dimers versus the pattern of grayed dimers), we multiply Eq. (8) by a factor of 2 to obtain the average probability that a (4×4) unit cell has a zigzag configuration.

An expression similar to Eq. (8) can also be obtained for the (4×4) inline dimer configuration (i.e., dimer sites 1 and 3 are occupied, with sites 2 and 4 vacant, or visa versa). Denoting this quantity $\langle p_r\rangle$ we renormalize p_z via

$$\tilde{p}_z = \frac{\langle p_z\rangle}{\langle p_z\rangle+\langle p_r\rangle}, \tag{9}$$

giving the order parameter of interest, $\tilde{p}_z$. By renormalizing with respect to only the dimer configurations consistent with the $\alpha 2(2\times 4)$, we prevent any contribution to the order pa-

rameter arising from local fluctuations in dimer concentration, which occasionally create instances of the $\beta 2(2\times4)$, especially at high temperature. The quantity $\tilde{p}_z$ then takes a value of one for perfect zigzag order, zero for perfect inline order, and 0.5 for a fully randomized configuration.

The quantity $\tilde{p}_z$ is shown in Fig. 11 for a number of temperatures, measured along the chemical-potential trajectory shown in Fig. 5 that passes only through the $\alpha 2(2\times4)$ phase field. We observe a strong preference for $[1\bar{1}0]$ zigzag order, peaking near 25% In composition and decreasing to a random distribution at high In concentration. The peak in the order parameter decreases in magnitude with increasing temperature due to thermally induced disorder, and the order parameter is almost flat at 500 °C, which is near typical growth temperatures for this system. This gives some indication of the temperature range over which order may be expected during layer-by-layer growth and after rapid quenching. Increased temperature also shifts the order-parameter peak to slightly higher In concentration (approaching 30% at 500 °C). The maximum is induced primarily by the preferential filling of $1s$ and $1's$ sites with In at low average In concentration. A single type 4 site per (4×4) cell is observed to fill with In, on average, so that the low-temperature maximum is at 25% In concentration. In conjunction with the propensity of In to occupy sites opposite the $\alpha 2(2\times4)$ row dimer, atomic-size mismatch strain is further reduced by maximizing the distance between In atoms. Along [110] this is mainly achieved by the separation of neighboring unit cells by the trench, but along $[1\bar{1}0]$ In atoms alternate their relative positions between neighboring unit cells to maximize their separation, forming a zigzag pattern. The single $\alpha 2(2\times4)$ row dimer does likewise but strongly prefers to sit opposite the In atoms. The net effect is two opposing zigzags along $[1\bar{1}0]$, one consisting of In pairs and the other consisting of row dimers. Figure 10(b) shows a microstate snapshot from a MC simulation illustrating zigzag ordering of $\alpha 2(2\times4)$ at 100 °C and 15% In composition. For comparison, Fig. 10(a) shows the pure GaAs surface, which has a random dimer arrangement.

The other region of greatest interest is that corresponding to the $h_{\alpha\beta}$ hybrid reconstruction, which is the small region of low dimer susceptibility, $\chi_{\mathrm{As,As}}$, along the $\alpha 2(2\times4)$-$\beta 2(2\times4)$ transition in Fig. 5. It is also highlighted as a prominent region of low adiabat density (labeled in Fig. 7). A microstate snapshot at a point within this region is shown in Fig. 10(c). Predicted and calculated ground-state configurations in this region have a strong tendency to alternate $\alpha 2(2\times4)$ and $\beta 2(2\times4)$ along both [110] and $[1\bar{1}0]$, and this unit-cell ordering is visible in the microstate snapshot. Due to the much higher In substitution energy in cation sites of $\beta 2(2\times4)$ relative to those of $\alpha 2(2\times4)$, a *lateral modulation* of surface In composition occurs between the In-rich $\alpha 2(2\times4)$ and In-poor $\beta 2(2\times4)$ when $h_{\alpha\beta}$ is stabilized. At lower In chemical potentials within the $h_{\alpha\beta}$ chemical-potential region, a large majority of In atoms migrate to unit cells of $\alpha 2(2\times4)$, with 56% of $\alpha 2(2\times4)$ cation sites filled with In in contrast to 22% of $\beta 2(2\times4)$ cation sites at the chemical-potential coordinate corresponding to Fig. 10(c). The 3, 4, and $4s$ sites do not play a significant role in this process due to the very low In occupancy of 3 sites and very high In occupancy of 4 and $4s$ sites, regardless of cell type. This composition modulation can be understood by considering the effects of alloying on reconstruction stability demonstrated in Sec. III A. As shown there, the $\alpha 2(2\times4)$ is much more stable under the addition of In than the $\beta 2(2\times4)$. This, along with the tendency of In atoms to mutually repel across unit-cell boundaries, helps to explain the $h_{\alpha\beta}$ as it appears in Fig. 10(c).

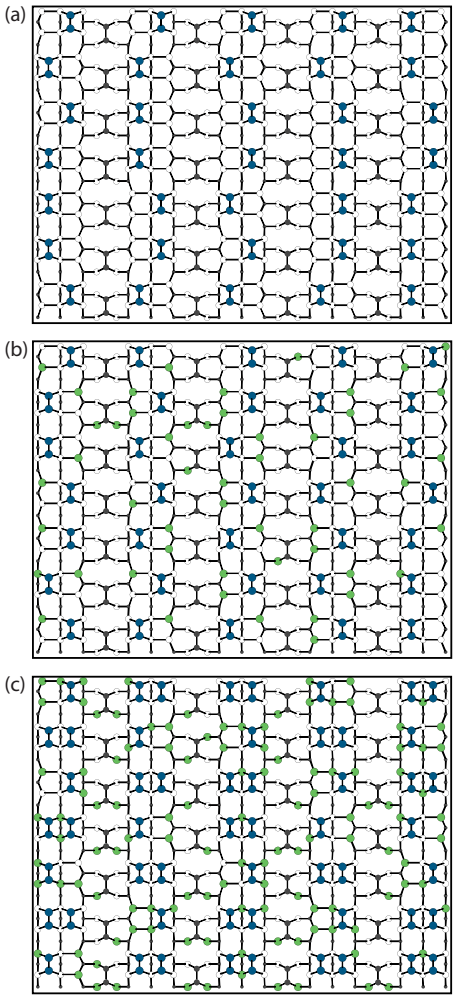

FIG. 10. (Color online) Microstate snapshots for the various points of chemical-potential space specified in Fig. 5. To emphasize order, In are light gray (green), Ga are white, and row dimers are dark gray (blue); all other As are black. (a) The $\alpha 2(2\times4)$ with no In, (b) the zigzag ordering of $\alpha 2(2\times4)$ with 15% In, and (c) the $h_{\alpha\beta}$ hybrid reconstruction at 75% dimer coverage and 37% In.

In addition to the regions of zigzag ordering and $h_{\alpha\beta}$, there are two additional features arising from short-range ordering in Fig. 8 that merit discussion. One occurs at 90% In in the $\alpha 2(2\times4)$ and the other occurs at 60–65 % in the $\beta 2(2\times4)$. We note, however, that these features are not necessarily of particular interest physically as they occur for chemical potentials where other reconstructions not considered here are likely to be stable relative to the $\alpha 2(2\times4)$ and $\beta 2(2\times4)$. In each instance, In fills all the available sites of the cation sublattice with the exception of those character-

ized by a high substitution energy. This results in many fewer energetically allowed arrangements of the cation sublattice than the combinatoric ideal and thus a change in convexity of the entropy. In the $\alpha 2(2\times 4)$ this occurs when all cation sites of the unit cell are filled except the very high-energy 3 sites. In the $\beta 2(2\times 4)$ it occurs when all but the 3 sites and one each of the 1 and 1′ sites are unfilled in the unit cell. These plateaus in filling are seen to some degree in Figs. 9(b) and 9(c), respectively. There is some ordering of the 1 and 1′ sites in the $\beta 2(2\times 4)$, which show a weak correlation along [210] but in large part, both orderings are caused by large differences in site substitution energies rather than interaction between sites.

IV. SUMMARY AND CONCLUSION

We have performed a first-principles study of surface reconstruction stability and order on the covalently bonded InAs/GaAs (001) surface at finite temperature, using a cluster expansion of the configurational energy together with Monte Carlo simulations. We have restricted our study to an examination of the effect of temperature and alloying on the relative stability between $\alpha 2(2\times 4)$ and $\beta 2(2\times 4)$ as well as the atomic-size mismatch strains arising from In substitution at GaAs surfaces and how these strains effect As dimer ordering. Because of the similarities observed among many III-V compounds and the tendency in general of directionally bonded surfaces to develop reconstructions, we can propose several phenomena that may deserve consideration in the engineering of nanostructured surfaces in these varied systems.

Size mismatch-driven surface destabilization. As seen in Fig. 5, substituting In atoms for the smaller Ga atoms destabilizes $\beta 2(2\times 4)$, resulting in the stability of $\alpha 2(2\times 4)$. It is expected that reconstruction stability exhibits a compositional dependence but in the case of size-mismatched alloys this effect is significantly more pronounced. This has been clearly observed experimentally as x is increased in $In_xGa_{1-x}As$ (001) alloys, causing a destabilization of both the $\beta 2(2\times 4)$ and the $c(4\times 4)$,[35] another III-V surface reconstruction with prominent anion dimers. The resulting surface reconstruction, which is not observed on either pure InAs or GaAs, has a $(n\times 3)$ surface repeat unit and has been observed to be robust over a wide range of growth conditions.[36,37] The precise atomic structure of this reconstruction, however, remains unclear.[37] The results presented here suggest that likely models for the reconstruction incorporate structural elements which would readily accept In, such as the cation backbonds found in the $\alpha 2(2\times 4)$.

Strain-induced order. We have shown the strong tendency to order that arises from alloying and size mismatch, as evidenced by preferential cation-site filling, changes in convexity of the configurational entropy, ensemble averaged site correlations, and Monte Carlo microstate snapshots. Surface order has been suggested previously as a mechanism for long-range bulk order in epitaxially grown ternary III-V films.[5] Although unstrained InAs and GaAs are completely immiscible over most temperatures of interest and only chalcopyrite-type ordering is predicted to be stable for epitaxially strained ternary III-V alloys, both CuPt- and CuAu-type alloy ordering have been observed on the face-centered-cubic bulk cation sublattice.[38,39] The proposed mechanism suggests that equilibrium or near-equilibrium surface order becomes kinetically trapped during layer-by-layer growth, yielding a reconstruction-dependent bulk order. Previous studies have focused on simple dimerized surfaces to examine the effect of dimers on surface order[7] or have studied pair correlations between substitutional sites in fully reconstructed surfaces[18] but computational limitations have largely prevented the full consideration of both temperature effects and multisite interactions for realistic surfaces. By considering the role of temperature, we have determined the temperature range over which surface order is expected to be most pronounced, as reflected in the temperature dependence of the zigzag order parameter (Fig. 11).Additionally, the consideration of multisite interactions has enabled the identification of a number of stable In-Ga orderings specific to the (2×4) reconstructions considered here, which may have relevance to bulk alloy order. While short-range order is quite strong in the alloyed surface studied here, long-range order on both the cation and dimer sublattices is weak at even moderate temperatures (200–500 °C), as determined from the lack of any strong minima in the configurational entropy and from analysis of microstate snapshots of the various surface orderings. If order on the bulk cation sublattice is indeed due to the kinetic trapping of surface cation order during growth,[7] we would expect the observed effect to be relatively short range, capturing only those correlations which are too strong to be overcome by thermal disorder at synthesis temperatures [e.g., the strong difference in occupancy of the 4 sites and 3 sites in the $\beta 2(2\times 4)$]. However, since we have only considered a thin InGaAs layer at the GaAs lattice parameter, it is unclear how the order would propagate during film growth or how surface order would manifest in lattice matched alloys.

Lateral composition modulation. We have also demonstrated the occurrence of a lateral composition modulation on the cation sublattice, driven by mutual ordering of the cation and dimer sublattices. This is most evident in the vicinity of

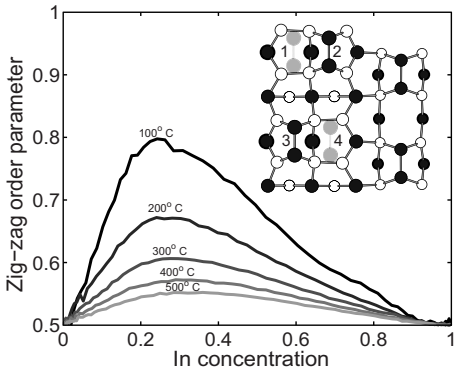

FIG. 11. The short-range dimer order parameter for zigzag ordering of the $\alpha 2(2\times 4)$ along [110]. It is shown with respect to surface In concentration at temperatures ranging from 100 to 500 °C along the chemical-potential trajectory corresponding to pure $\alpha 2(2\times 4)$. The fully ordered configuration is shown as an inset, with row dimer sites numbered and vacant sites indicated by gray dimers.

75% dimer coverage, where the $h_{\alpha\beta}$ hybrid reconstruction occurs, characterized by locally increased In concentrations at $\alpha 2(2\times 4)$ cells, where substitution is energetically preferred. Yet again a consequence of the strong intersublattice interaction, this ordering results in relatively strong cation concentration fluctuations over larger length scales than any of the other predicted orderings. Conceivably, similar regimes may exist for other reconstructions but composition modulation may manifest differently in other systems, depending on symmetry and repeat units. Hence other systems may exhibit hybrid reconstructions with different geometries and modulation length scales. Although atomic-scale cation concentration is difficult to measure in practice, transmission electron microscopy (TEM) studies of InGaP films, for example, have shown what are thought to be regions of high and low In concentration resulting from variations in atomic surface structure.[40] These composition fluctuations, termed branch defects, can have a measurable effect on device performance by pinning dislocations, which act as nonradiative recombination sites. Additionally, reconstructions have been directly implicated in lateral composition modulation in work by Pearson *et al.*,[41] which demonstrated a correlation between lateral composition modulation identified using TEM with periodic variations in surface reconstruction observed using scanning tunneling microscopy in the InGaAs system.

ACKNOWLEDGMENTS

We gratefully acknowledge support from DOE/BES (Grant No. ER 46172). This work was performed in part at the US Department of Energy, Center for Integrated Nanotechnologies, at Los Alamos National Laboratory (Contract DE-AC52–06NA25396) and Sandia National Laboratories (Contract DE-AC04-94AL85000).

*avdv@umich.edu

[1] P. Kratzer, E. Penev, and M. Scheffler, Appl. Surf. Sci. **216**, 436 (2003).
[2] G. A. Somorjai, Annu. Rev. Phys. Chem. **45**, 721 (1994).
[3] G. Zhou and J. Yang, J. Mater. Res. **20**, 1684 (2005).
[4] U. Welp, V. K. Vlasko-Vlasov, X. Liu, J. K. Furdyna, and T. Wojtowicz, Phys. Rev. Lett. **90**, 167206 (2003).
[5] S. Froyen and A. Zunger, Phys. Rev. B **53**, 4570 (1996).
[6] Z. Kollonitsch, H.-J. Schimper, U. Seidel, K. Möller, S. Neumann, F.-J. Tegude, F. Willig, and T. Hannappel, J. Cryst. Growth **287**, 536 (2006).
[7] R. Osório, J. E. Bernard, S. Froyen, and A. Zunger, Phys. Rev. B **45**, 11173 (1992).
[8] T. Hofmann, V. Gottschalch, and M. Schubert, Phys. Rev. B **66**, 195204 (2002).
[9] B. Voigtländer, Surf. Sci. Rep. **43**, 127 (2001).
[10] J. E. Bickel, N. A. Modine, A. Van der Ven, and J. M. Millunchick, Appl. Phys. Lett. **92**, 062104 (2008).
[11] W. Barvosa-Carter, R. S. Ross, C. Ratsch, F. Grosse, J. H. G. Owen, and J. J. Zinck, Surf. Sci. **499**, L129 (2002).
[12] W. Schmidt, Appl. Phys. A: Mater. Sci. Process. **75**, 89 (2002).
[13] C. Ratsch, W. Barvosa-Carter, F. Grosse, J. H. G. Owen, and J. J. Zinck, Phys. Rev. B **62**, R7719 (2000).
[14] S.-H. Lee, W. Moritz, and M. Scheffler, Phys. Rev. Lett. **85**, 3890 (2000).
[15] T. J. Krzyzewski, P. B. Joyce, G. R. Bell, and T. S. Jones, Surf. Sci. **517**, 8 (2002).
[16] A. Chakrabarti, P. Kratzer, and M. Scheffler, Phys. Rev. B **74**, 245328 (2006).
[17] M. D. Pashley, Phys. Rev. B **40**, 10481 (1989).
[18] J.-H. Cho, S. B. Zhang, and A. Zunger, Phys. Rev. Lett. **84**, 3654 (2000).
[19] S. Franchi, A. Bosacchi, F. Colonna, P. Pascarella, P. Allegri, and V. Avanzini, J. Cryst. Growth **150**, 185 (1995).
[20] C. Dorin and J. M. Millunchick, J. Appl. Phys. **91**, 237 (2002).
[21] V. Ozoliņš, M. Asta, and J. J. Hoyt, Phys. Rev. Lett. **88**, 096101 (2002).
[22] B. Yang, T. Muppidi, V. Ozoliņš, and M. Asta, Phys. Rev. B **77**, 205408 (2008).
[23] J. M. Sanchez, F. Ducastelle, and D. Gratias, Physica A: Statistical and Theoretical Physics **128**, 334 (1984).
[24] D. De Fontaine, in *Solid State Physics*, edited by H. Ehrenreich and D. Turnbull (Academic, New York, 1994), p. 33.
[25] A. Zunger, in *Statics and Dynamics of Alloy Phase Transformations*, NATO Advanced Studies Institute, Series B: Physics, Vol. 319, edited by P. E. A. Turchi and A. Gonia (Plenum, New York, 1992), p. 361.
[26] P. D. Tepesch, G. D. Garbulsky, and G. Ceder, Phys. Rev. Lett. **74**, 2272 (1995).
[27] B. C. Han, A. Van der Ven, G. Ceder, and B.-J. Hwang, Phys. Rev. B **72**, 205409 (2005).
[28] G. Kresse and J. Furthmüller, Phys. Rev. B **54**, 11169 (1996).
[29] D. Vanderbilt, Phys. Rev. B **41**, 7892 (1990).
[30] D. M. Ceperley and B. J. Alder, Phys. Rev. Lett. **45**, 566 (1980).
[31] J. P. Perdew and A. Zunger, Phys. Rev. B **23**, 5048 (1981).
[32] G. Hart, V. Blum, M. Walorski, and A. Zunger, Nature Mater. **4**, 391 (2005).
[33] A. van de Walle and G. Ceder, J. Phase Equilib. **23**, 348 (2002).
[34] N. Metropolis, A. W. Rosenbluth, M. N. Rosenbluth, A. H. Teller, and E. Teller, J. Chem. Phys. **21**, 1087 (1953).
[35] M. Sauvage-Simkin, R. Pinchaux, J. Massies, P. Claverie, N. Jedrecy, J. Bonnet, and I. K. Robinson, Phys. Rev. Lett. **62**, 563 (1989).
[36] J. Mirecki Millunchick, A. Riposan, B. J. Dall, C. Pearson, and B. G. Orr, Surf. Sci. **550**, 1 (2004).
[37] P. Bone, J. Ripalda, G. Bell, and T. Jones, Surf. Sci. **600**, 973 (2006).
[38] T.-Y. Seong, A. G. Norman, G. R. Booker, and A. G. Cullis, J. Appl. Phys. **75**, 7852 (1994).
[39] O. Ueda, Y. Nakata, and T. Fujii, Appl. Phys. Lett. **58**, 705 (1991).
[40] A. Y. Kim, W. S. McCullough, and E. A. Fitzgerald, J. Vac. Sci. Technol. B **17**, 1485 (1999).
[41] C. Pearson, C. Dorin, J. M. Millunchick, and B. G. Orr, Phys. Rev. Lett. **92**, 056101 (2004).